

# SCIENTIFIC REPORTS



OPEN

## The In-Plane Anisotropy of $\text{WTe}_2$ Investigated by Angle-Dependent and Polarized Raman Spectroscopy

Received: 23 March 2016

Accepted: 15 June 2016

Published: 11 July 2016

Qingjun Song<sup>1,2</sup>, Xingchen Pan<sup>3,4</sup>, Haifeng Wang<sup>3,4</sup>, Kun Zhang<sup>1,2</sup>, Qinghai Tan<sup>5</sup>, Pan Li<sup>6</sup>, Yi Wan<sup>1,2</sup>, Yilun Wang<sup>1,2</sup>, Xiaolong Xu<sup>1,2</sup>, Miaoling Lin<sup>5</sup>, Xianggang Wan<sup>3,4</sup>, Fengqi Song<sup>3,4</sup> & Lun Dai<sup>1,2</sup>

Tungsten ditelluride ( $\text{WTe}_2$ ) is a semi-metallic layered transition metal dichalcogenide with a stable distorted 1T phase. The reduced symmetry of this system leads to in-plane anisotropy in various materials properties. We have systemically studied the in-plane anisotropy of Raman modes in few-layer and bulk  $\text{WTe}_2$  by angle-dependent and polarized Raman spectroscopy (ADPRS). Ten Raman modes are clearly resolved. Their intensities show periodic variation with sample rotating. We identify the symmetries of the detected modes by quantitatively analyzing the ADPRS results based on the symmetry selection rules. Material absorption effect on the phonon modes with high vibration frequencies is investigated by considering complex Raman tensor elements. We also provide a rapid and nondestructive method to identify the crystallographic orientation of  $\text{WTe}_2$ . The crystallographic orientation is further confirmed by the quantitative atomic-resolution force image. Finally, we find that the atomic vibrational tendency and complexity of detected modes are also reflected in the shrinkage degree defined based on ADPRS, which is confirmed by corresponding density functional calculation. Our work provides a deep understanding of the interaction between  $\text{WTe}_2$  and light, which will benefit in future studies about the anisotropic physical properties of  $\text{WTe}_2$  and other in-plane anisotropic materials.

Transition metal dichalcogenides (TMDs) have attracted a lot of attention because of their emerging and remarkable electrical, optical and mechanical properties<sup>1,2</sup>. In contrast to the widely studied TMDs like  $\text{MoS}_2$ ,  $\text{WS}_2$ ,  $\text{MoSe}_2$ ,  $\text{WSe}_2$  and  $\text{MoTe}_2$ <sup>3–5</sup>, which are in-plane isotropous,  $\text{WTe}_2$  crystallizes in a distorted structure with an octahedral coordination around the metal, referred to as Td-polytype<sup>6</sup>. The recent discovery of non-saturating giant positive magnetoresistance and excellent thermoelectric behaviors in  $\text{WTe}_2$  arouses great interest in this material<sup>7–9</sup>. In addition,  $\text{WTe}_2$  is predicted to be a novel type of topological semimetal for further quantum transport studies<sup>10</sup>. The Td- $\text{WTe}_2$  is constituted with triple-layer covalently bonded Te-W-Te atomic planes stacking along the *c*-axis through van der Waals interactions, as shown in Fig. 1a,b. The Td- $\text{WTe}_2$  is strongly distorted from the ideal hexagonal net, because the off-centering W atoms form the slightly buckled W-W zigzag chains along the *a*-axis of the orthorhombic unit cell, as shown in Fig. 1c. The reduced crystal symmetry of  $\text{WTe}_2$  leads to the strong in-plane anisotropy.

Raman spectroscopy of both few-layer and bulk  $\text{WTe}_2$  was reported recently, which was crucial first step for  $\text{WTe}_2$  crystal structure characterization<sup>6,11–14</sup>. However, in order to further study the particular property of  $\text{WTe}_2$  and exploit related novel electronic and optoelectronic devices, more detailed study about few-layer and bulk  $\text{WTe}_2$  Raman spectra is still needed. In this work, we investigate the detailed Raman responses of both few-layer and bulk  $\text{WTe}_2$  flakes using the high-resolution angle-dependent and polarized Raman spectroscopy (ADPRS). The detected Raman modes are much more compared with the previous literatures<sup>6,11–13</sup>. By combining the

<sup>1</sup>State Key Lab for Mesoscopic Physics and School of Physics, Peking University, Beijing, 100871, China.

<sup>2</sup>Collaborative Innovation Center of Quantum Matter, Beijing, 100871, China. <sup>3</sup>National Laboratory of Solid State Microstructures, College of Physics, Nanjing University, Nanjing, 210093, China. <sup>4</sup>Collaborative Innovation Center of Advanced Microstructures, Nanjing University, Nanjing, 210093, China. <sup>5</sup>State Key Laboratory of Superlattices and Microstructures, Institute of Semiconductors, Chinese Academy of Sciences, Beijing, 100083, China. <sup>6</sup>MOE Key Laboratory for Nonequilibrium Synthesis and Modulation of Condensed Matter, Xi'an Jiaotong University, Xi'an, 710049, P. R. China. Correspondence and requests for materials should be addressed to F.S. (email: songfengqi@nju.edu.cn) or L.D. (email: lundai@pku.edu.cn)

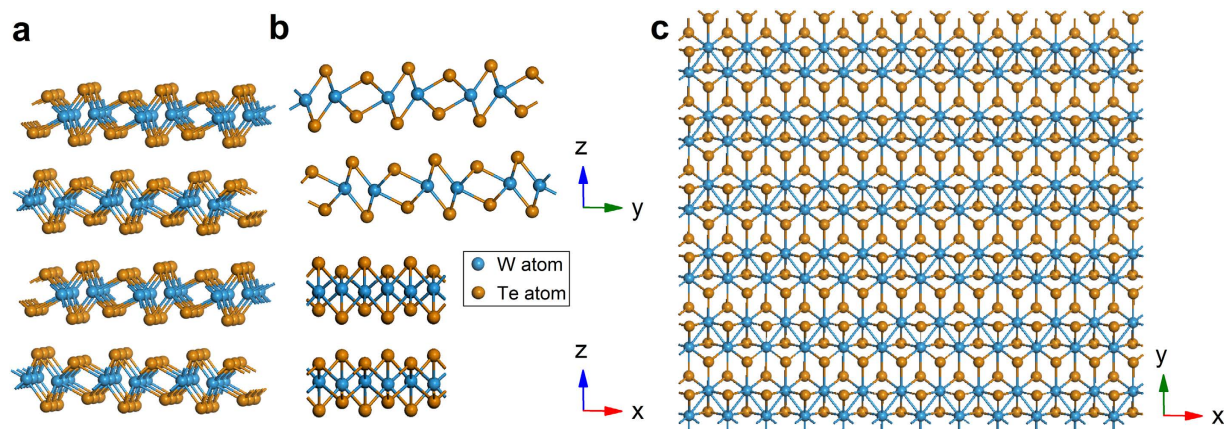


**Figure 1.** Crystalline structure of Td-WTe<sub>2</sub>, with (a) perspective view, (b) front view and side views, (c) top view.

symmetry analysis of the ADPRS results and the first principle calculation, we can accurately identify the symmetries of the detected modes and obtain the relation between their symmetries and lattice vibrations. We also identify the crystalline orientation of the WTe<sub>2</sub> flakes based on the “in-plane anisotropy”, which is a precise and non-destructive all-optical method. Our work provides a deep understanding of the interaction between WTe<sub>2</sub> and light, which will benefit in future studies about the anisotropic optical, electrical, and mechanical properties of WTe<sub>2</sub> and other in-plane anisotropic materials<sup>15–35</sup>.

## Results and Discussion

The Td-WTe<sub>2</sub> bulk crystal used in this work was grown by the chemical vapor transport (CVT) method (more details in Method). The mono- and few-layer WTe<sub>2</sub> were mechanically exfoliated on 300 nm SiO<sub>2</sub>/Si and quartz substrates (Supplementary Fig. S1) from the crystal. Figure 2a shows the optical microscope image of an as-exfoliated few-layer WTe<sub>2</sub>. Usually a well-defined edge (indicated by the white double-headed arrow) is naturally formed after exfoliation, due to the small cleave energy along the *a*-axis (*i.e.*, the direction along the W-W chains). This is further confirmed by the quantitative atomic resolution force image probed by high-resolution atomic force microscopy (HR-AFM)<sup>36</sup>. Here, we define the *a*-axis as *x*-axis, the in plane direction perpendicular to it as *y*-axis, and the direction perpendicular to the 2D plane (*c*-axis) as *z*-axis. Figure 2b is an AFM image of the few-layer WTe<sub>2</sub> (the red box area) in Fig. 2a. The corresponding HR-AFM image (the green box area) is shown in Fig. 2c. The smoothed HR-AFM image after the fast Fourier transform (FFT) is depicted in Fig. 2d. We can observe clearly one dimensional atomic chains parallel to the well-defined edge shown in Fig. 2a. The inset in Fig. 2d is the FFT image, where the distorted hexagon shape originates from the two different tungsten-tellurium bond lengths (2.7 Å and 2.8 Å). The height variation induced by the protruding tellurium atoms (highlighted in yellow in the inset) perpendicular to the one dimensional chains is shown in Fig. 2e. The average peak distance is about 6.65 Å, close to the lattice constant *b*.

In the ADPRS measurement, a WTe<sub>2</sub> flake on SiO<sub>2</sub>/Si substrate was initially placed with an arbitrary angle  $\theta_0$  between the *x*-axis and horizontal direction. Herein,  $\theta_0$  can be used to denote the crystalline orientation. We define  $\theta_0$  to be positive (negative) value, when the *x*-axis is clockwise (anti-clockwise) compared to the horizontal direction (more details in Method and Supplementary Fig. S2). Figure 3a shows the Raman spectra of WTe<sub>2</sub> in the un-, parallel- and cross-polarized configurations measured at an angle with the maximum number of Raman active modes. Altogether, ten Raman modes can be resolved. All of them can be well fitted by Lorentzian lineshape. Figure 3b–d show the angular dependences of the normalized Raman intensity spectra in the un-, parallel- and cross-polarized configurations, respectively. The sample rotation angle is in a range of 0–360°. The highest peak in each spectrum is used for normalization. We can see that, in the parallel-polarized configuration, the modes at ~80, 133, 135, 137 and 212 cm<sup>-1</sup> yield 2-lobed shape with two maximum intensity angles at about 65° and 245°; the modes at ~117 and 164 cm<sup>-1</sup> yield 2-lobed shape with two maximum intensity angles at about 155° and 335°; and the modes at ~91, 112 and 161 cm<sup>-1</sup> yield 4-lobed shape with four maximum intensity angles at about 20°, 110°, 200° and 290°. In the cross-polarized configuration, all modes yield 4-lobed shape. The four maximum intensity angles for the modes at ~91, 112 and 161 cm<sup>-1</sup> are  $\theta = 65^\circ, 155^\circ, 245^\circ$  and  $335^\circ$ , and those for the rest ones are 20°, 110°, 200° and 290°. In addition, we can see that the intensities of the three neighbored modes at 133, 135 and 137 cm<sup>-1</sup> have similar angular dependent relations; while those of the two neighbored modes at 161 and 164 cm<sup>-1</sup> have different angular dependent relations. The related angular dependent evolutions of these detected modes in the rotation angle range of 0–90° under the three polarized configurations are shown in Supplementary Figs S4–7, respectively. The ADPRS results for WTe<sub>2</sub> with four representative different thicknesses (~3 nm, 10 nm, 25 nm and 40 nm) are shown in Supplementary Fig. S3. The results show that the anisotropic Raman spectra of WTe<sub>2</sub> flakes have no clear thickness ( $\geq 3$  nm) dependence.

We can quantitatively analyze these observed anisotropic phenomena, based on the group theory, Raman tensors and density functional theory (DFT) calculations. According to symmetry analysis, the bulk Td-WTe<sub>2</sub> belongs to the space group Pmn2<sub>1</sub> and point group C<sub>2v</sub><sup>7,11,37</sup>. The unit cell of bulk Td-WTe<sub>2</sub> contains two tungsten atoms and four tellurium atoms. There are 33 normal optical phonon modes at the Brillion zone center  $\Gamma$  point, with irreducible representation as  $\Gamma_{\text{bulk}} = 11A_1 + 6A_2 + 5B_1 + 11B_2$ , where all the vibration modes are Raman

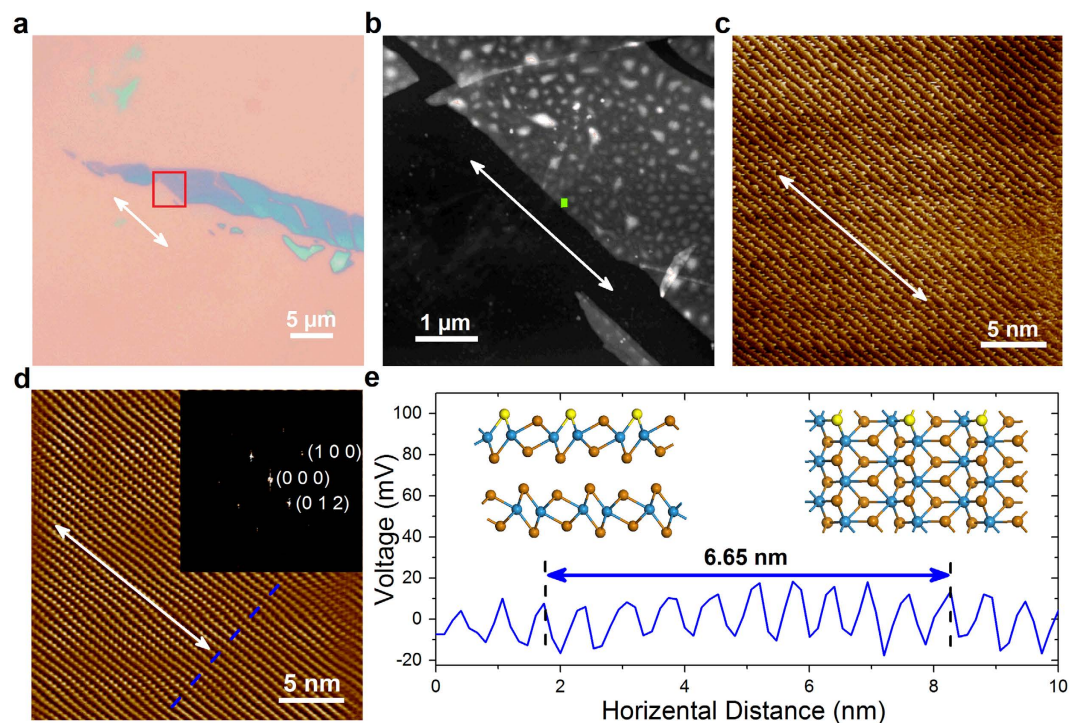


**Figure 2.** (a) Optical microscope image of the measured exfoliated  $\text{WTe}_2$  flake on  $\text{SiO}_2/\text{Si}$  substrate. The white double-headed arrow indicates the well-defined edge, which is naturally formed after exfoliation. (b) AFM image of the red box area of the  $\text{WTe}_2$  depicted in (a). (c) HR-AFM image of the green box area of the  $\text{WTe}_2$  depicted in (b). (d) The smoothed HR-AFM image after FFT. The FFT image is shown in the inset. (e) The height variation profile perpendicular to the one dimensional chain along the dashed line in (d). The direction of well-defined edge in (a,b) and the direction along one dimensional chain in (c,d) are represented by white double arrows.

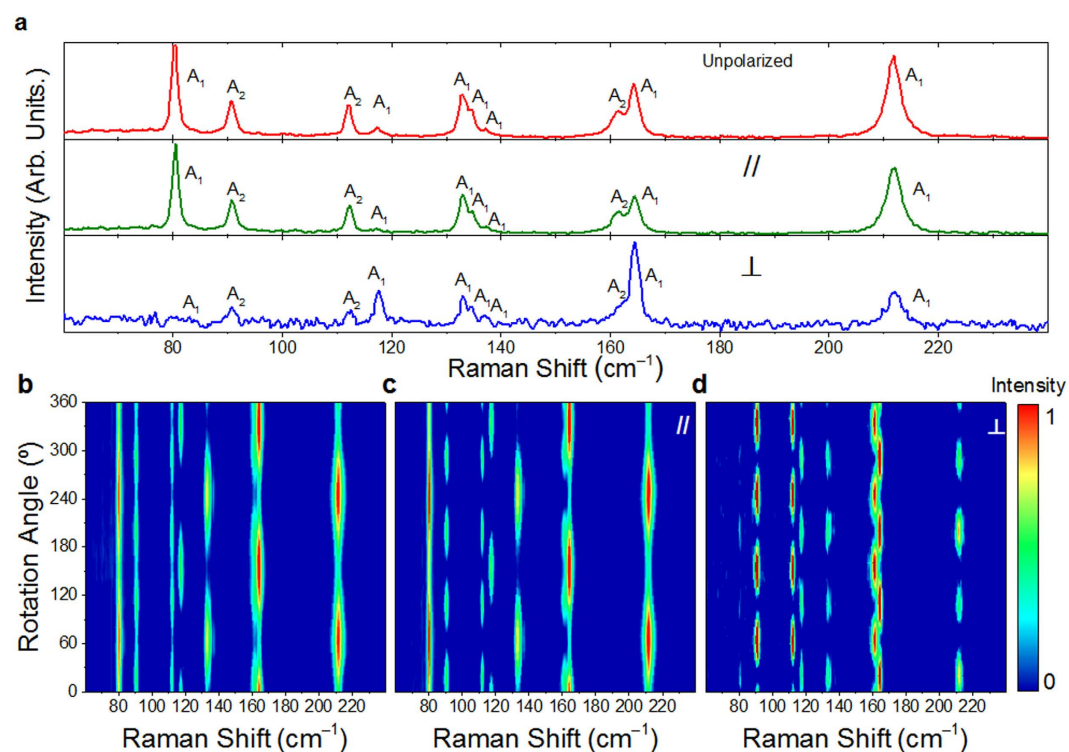


**Figure 3.** (a) Normalized Raman spectra measured at an angle where all modes appear in un-, parallel- and cross-polarized configurations. Angular dependence of the normalized Raman intensity spectra for the  $\text{WTe}_2$  flake measured in (b) un-polarized, (c) parallel-polarized and (d) cross-polarized configurations.

$$\begin{aligned}\tilde{\mathbf{R}}(A_1) &= \begin{pmatrix} a & 0 & 0 \\ 0 & b & 0 \\ 0 & 0 & c \end{pmatrix} & \tilde{\mathbf{R}}(A_2) &= \begin{pmatrix} 0 & d & 0 \\ d & 0 & 0 \\ 0 & 0 & 0 \end{pmatrix} \\ \tilde{\mathbf{R}}(B_1) &= \begin{pmatrix} 0 & 0 & 0 \\ 0 & 0 & e \\ 0 & e & 0 \end{pmatrix} & \tilde{\mathbf{R}}(B_2) &= \begin{pmatrix} 0 & 0 & f \\ 0 & 0 & 0 \\ f & 0 & 0 \end{pmatrix}\end{aligned}$$

**Figure 4. Raman tensor forms for all Raman active modes in bulk WTe<sub>2</sub>.**

active. The  $11A_1$ ,  $5B_1$  and  $11B_2$  modes are also infrared active. There exists a correlation between the Raman tensors of bulk and few-layer WTe<sub>2</sub> (more details in Supplementary Information). For simplicity, we use the Raman tensors of bulk WTe<sub>2</sub> (Fig. 4) to do the analysis<sup>11,12</sup>.

According to the classical Placzek approximation, the Raman intensity of a phonon mode can be written as<sup>38</sup>:

$$I \propto |e_i \cdot \tilde{\mathbf{R}} \cdot e_s|^2 \quad (1)$$

where  $e_i$  and  $e_s$  are the electric polarization unitary vectors of the incident and scattered lights, respectively, and  $\tilde{\mathbf{R}}$  is the Raman tensor. The Raman tensors for all Raman active modes in bulk WTe<sub>2</sub> are given in Fig. 4. Based on the Cartesian coordinates denoted above, the  $e_i$  and  $e_s$  are fixed in  $xy$  plane. For a sample with rotation angle of  $\theta$  (clockwise rotation, as shown in Fig. S2),  $e_i = (\cos(\theta + \theta_0) \sin(\theta + \theta_0) 0)$  for the incident light, and  $e_s = (\cos(\theta + \theta_0) \sin(\theta + \theta_0) 0)$  and  $(-\sin(\theta + \theta_0) \cos(\theta + \theta_0) 0)$  for the scattered light in the parallel- and cross-polarized configurations, respectively. A phonon mode can only be detected when  $|e_i \cdot \tilde{\mathbf{R}} \cdot e_s|^2$  has non-zero value. Therefore, in the backscattering geometry, only  $A_1$  and  $A_2$  Raman modes can be observed. Using the above defined unitary vectors  $e_i$  and  $e_s$ , as well as the Raman tensors of  $A_1$  and  $A_2$  modes, we can obtain the angular dependent intensity expressions for the  $A_1$  and  $A_2$  modes to be:

$$I_{A_1}^{\parallel} \propto a^2 \left| 1 + \left( \frac{b}{a} - 1 \right) \sin^2(\theta + \theta_0) \right|^2 \quad (2)$$

$$I_{A_1}^{\perp} \propto \frac{1}{4} a^2 \left( \frac{b}{a} - 1 \right)^2 \sin^2 2(\theta + \theta_0) \quad (3)$$

$$I_{A_2}^{\parallel} \propto d^2 \sin^2 2(\theta + \theta_0) \quad (4)$$

$$I_{A_2}^{\perp} \propto d^2 \cos^2 2(\theta + \theta_0). \quad (5)$$

As the initial angle  $\theta_0$  is fixed, the intensity of  $A_1$  or  $A_2$  mode is a function of the corresponding elements of Raman tensor ( $a$  and  $b$ ) and the rotation angle  $\theta$ . In the parallel-polarized configuration, the angular dependence for the intensity of  $A_1$  mode has two cases, both of which have a variation period of  $180^\circ$ . For  $A_1$  mode with  $a > b$ , the maximum intensity appears at  $\theta = 180^\circ - \theta_0$  and  $360^\circ - \theta_0$ , corresponding to the incident light polarization parallel to the W-W chains. On the contrary, the minimum intensity appears at  $\theta = 90^\circ - \theta_0$  and  $270^\circ - \theta_0$ , corresponding to the incident light polarization perpendicular to the W-W chains. For the  $A_1$  mode with  $a < b$ , the maximum intensity angles are  $\theta = 90^\circ - \theta_0$  and  $270^\circ - \theta_0$ , and the minimum intensity angles are  $\theta = 180^\circ - \theta_0$  and  $360^\circ - \theta_0$ , corresponding to the incident light polarization perpendicular and parallel to the W-W chains, respectively. In the parallel-polarized configuration, the angular dependence for the intensity of  $A_2$  mode has a variation period of  $90^\circ$  with the maximum intensity at  $\theta = 45^\circ - \theta_0$ ,  $135^\circ - \theta_0$ ,  $225^\circ - \theta_0$  and  $315^\circ - \theta_0$ , and the minimum intensity at  $\theta = 90^\circ - \theta_0$ ,  $180^\circ - \theta_0$ ,  $270^\circ - \theta_0$  and  $360^\circ - \theta_0$ . In the cross-polarized configuration, both of  $A_1$  and  $A_2$  modes have a variation period of  $90^\circ$ . The intensity of  $A_1$  mode ( $A_2$  mode) reaches its maximum (minimum) at  $\theta = 45^\circ - \theta_0$ ,  $135^\circ - \theta_0$ ,  $225^\circ - \theta_0$  and  $315^\circ - \theta_0$ , and reaches its minimum (maximum) at  $\theta = 90^\circ - \theta_0$ ,  $180^\circ - \theta_0$ ,  $270^\circ - \theta_0$  and  $360^\circ - \theta_0$ . In addition, the normalized Raman intensities of the ten detected modes (except for  $A_2$  modes) in un-polarized configuration exhibit similar angular dependences to those in parallel-polarized configuration, as shown in Supplementary Fig. S8. It is worth noting that, as sample rotates, the full width at half maximum (FWHM) of each detected mode keeps almost constant, as shown in Supplementary Fig. S9.

According to the above analysis, we can use the ADPRS to identify the symmetries of the detected modes. The intensity variation periods for  $A_1$  modes are  $180^\circ$  and  $90^\circ$  in parallel- and cross-polarized configurations, respectively, while those for  $A_2$  phonon modes are  $90^\circ$  in both configurations. Therefore, seven phonon modes located at  $\sim 80$ ,  $117$ ,  $133$ ,  $135$ ,  $137$ ,  $164$  and  $212 \text{ cm}^{-1}$  belong to  $A_1$  modes, and three modes located at  $\sim 91$ ,  $112$  and  $161 \text{ cm}^{-1}$  belong to  $A_2$  modes. In addition, we find that when the incident polarization is parallel to the well-defined edge (*i.e.* parallel to the W-W chains) of the sample, the Raman modes at  $117$  and  $164 \text{ cm}^{-1}$  reach their maximum intensities. Therefore, we assign them to  $A_1$  modes with  $a > b$ . The rest  $A_1$  modes are with  $a < b$ . The lattice vibrations of

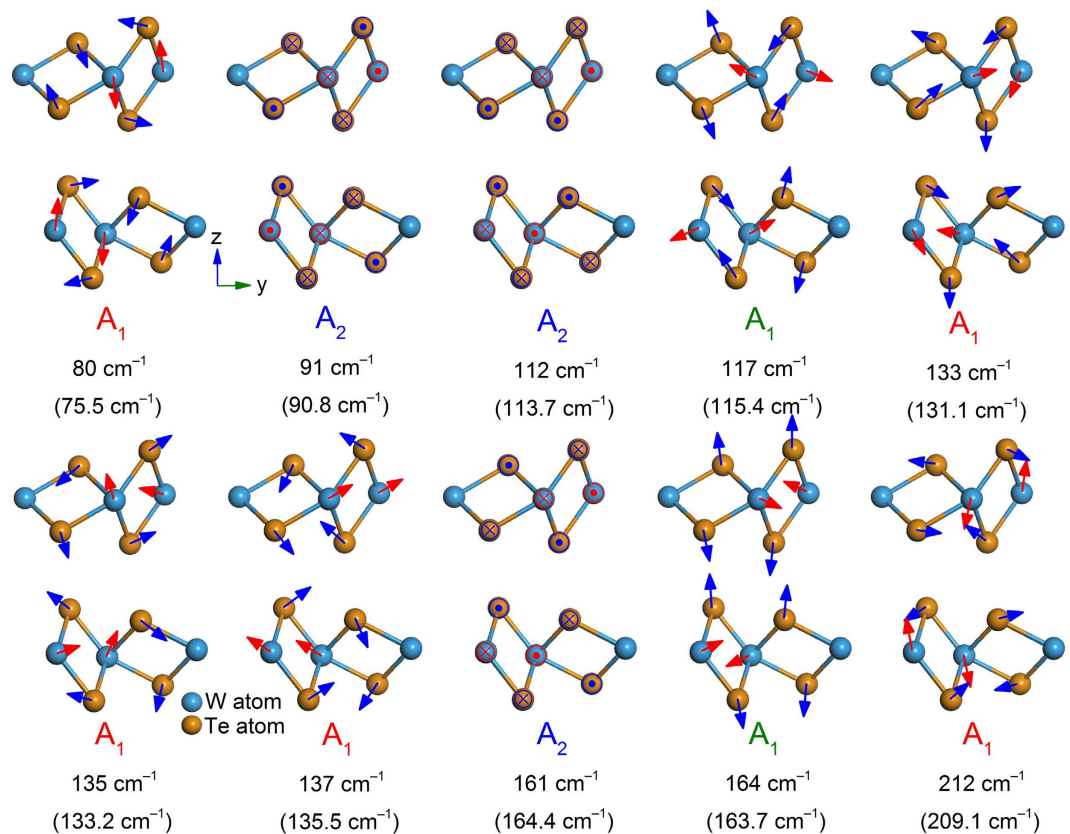


**Figure 5.** The calculated atomic displacements for the lattice vibrations of the ten detected modes in  $\text{WTe}_2$ , together with their corresponding irreducible representations. The theoretical frequency is given below its experimental counterpart in each plot. The motions of W (Te) atoms are presented by red (blue) arrows.

all phonon modes are calculated by the density functional theory (DFT, more details in Method, Supplementary Fig. S11 and Table S1), and atomic displacements of detected ones are shown in Fig. 5. Because monolayer  $\text{WTe}_2$  (with space group  $P21/m$  and point group  $C_{2h}^2$ ) has different crystal symmetry with the bulk one, the 2-lobed modes in monolayer  $\text{WTe}_2$  can be labelled as  $A_g$ , and the 4-lobed ones can be labelled as  $B_g$ . Notably, there is no odd and even layer number dependence of crystal symmetry for  $\text{WTe}_2$ . Therefore, for  $N$ -layer  $\text{WTe}_2$  ( $N \geq 2$ , with space group  $Pm$  and point group  $C_s^1$ ), the 2-lobed and 4-lobed modes can be labelled as  $A'$  and  $A''$ , respectively.

Notably, according to above results, we can use the maximum intensity of the mode at  $\sim 164 \text{ cm}^{-1}$  in un- and parallel-polarized configurations to identify the crystallographic orientation (*i.e.* the direction of W-W chains) rapidly and nondestructively. This is important in case that the well-defined edge of a few-layer  $\text{WTe}_2$  cannot be easily identified by the optical microscopy. In our case, it is represented by  $\theta_0 \sim 25^\circ$ . The angular dependence of the normalized Raman intensities for the ten detected modes in the parallel- and cross-polarized configurations are shown in the polar plots in Fig. 6a–j. Notably, since the opposite angular dependent relations for  $A_1$  modes with  $a < b$  and  $a > b$ , their intensity ratio shows a clearer 2-lobed characteristic with sample rotating, as shown in Fig. 6k. By curving fitting Fig. 6k, we can obtain a more accurate  $\theta_0$  to be  $27.5^\circ$ . The angular dependences of the Raman intensity ratios between other  $A_1$  and  $A_2$  modes, which are also helpful for identifying the crystallographic orientation, are shown in Supplementary Fig. S10.

It is worth noting that, the polar plots of  $A_1$  modes with higher frequencies (164 and  $212 \text{ cm}^{-1}$ ) in Fig. 6i,j cannot be well fitted by equation (2) (the blue and purple lines are the corresponding fitting results). In order to explain this, we consider the light absorption effect on the Raman tensor elements<sup>38,39</sup>. In an absorptive material, the elements of the Raman tensor should be complex numbers, with real and imaginary parts. In this case, the tensor elements of  $A_1$  and  $A_2$  can be written as

$$a = |a|e^{i\phi_a}, b = |b|e^{i\phi_b}, d = |d|e^{i\phi_d} \quad (6)$$

where  $\phi_a$ ,  $\phi_b$  and  $\phi_d$  are the corresponding phases. Substituting in equation (1) with the unitary vectors  $e_i$  and  $e_s$  and the above Raman tensor elements, we can modify the angular dependent intensity expressions of the  $A_1$  and  $A_2$  modes as:

$$I_{A_1}^{\parallel} \propto |a|^2 \left[ \left| 1 + \left( \frac{|b|}{|a|} - 1 \right) \sin^2(\theta + \theta_0) \right|^2 + \frac{1}{2} \frac{|b|}{|a|} \sin^2 2(\theta + \theta_0) (\cos \phi_{ba} - 1) \right] \quad (7)$$

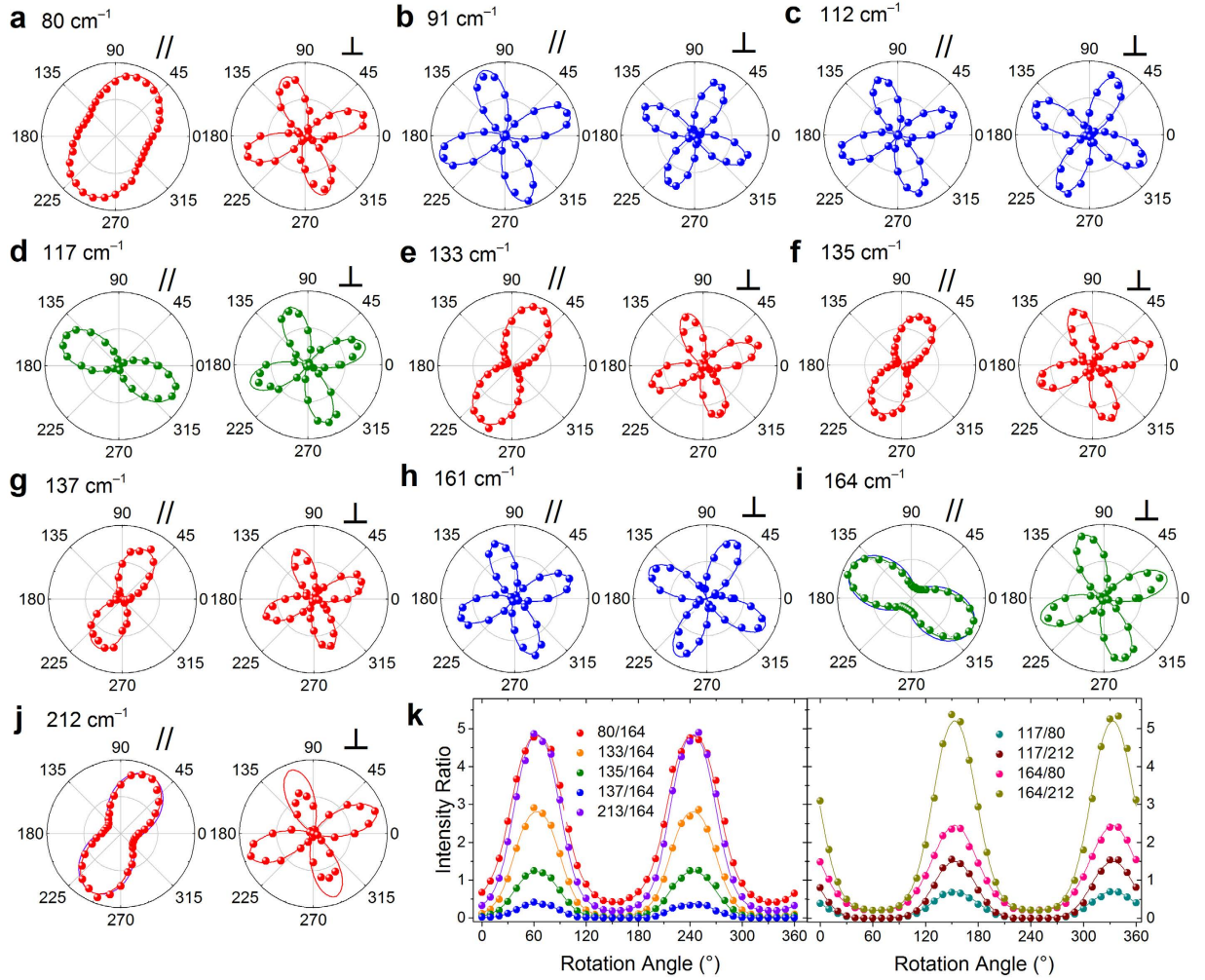


**Figure 6.** Angular dependence of the Raman intensities for the detected ten modes (a–j) in the parallel and cross polarization configurations. The experimental data are the scattered dots, and the curve fitting results are the solid lines. The intensity for each mode is normalized to its maximum value. Three types of modes, which have different angular dependent relations are colored in red, green and blue, respectively. (k) Angular dependence of the Raman intensity ratio for  $A_1$  modes with  $a < b$  and  $a > b$  in the parallel-polarized configuration. The curving fitting results are the solid lines.

$$I_{A_1}^{\perp} \propto |a|^2 \left[ \frac{1}{4} \left( \frac{|b|}{|a|} - 1 \right)^2 + \frac{1}{2} \frac{|b|}{|a|} (1 - \cos \phi_{ba}) \right] \sin^2 2(\theta + \theta_0) \quad (8)$$

$$I_{A_2}^{\parallel} \propto |d|^2 \sin^2 2(\theta + \theta_0) \quad (9)$$

$$I_{A_2}^{\perp} \propto |d|^2 \cos^2 2(\theta + \theta_0) \quad (10)$$

where  $\phi_{ba} = \phi_b - \phi_a$  is the phase difference between the Raman tensor elements  $b$  and  $a$ . The expressions for  $A_2$  modes (equations 9 and 10) are identical to their counterparts (equations 4 and 5) obtained considering only real part of the Raman tensor elements. However, the expressions for  $A_1$  modes are different. We can see that the absorption effect on the ADPRS reflects in phase difference. The angular dependent intensities of  $A_1$  modes at 164 and 212  $\text{cm}^{-1}$  can be well fitted by equations (7) and (8), as shown in Fig. 6i,j.

To further characterize the vibration direction of atoms for these detected modes. We choose defined  $x$ ,  $y$  and  $z$  axes as the reference directions. Compared with the typical atomic displacements in 2H-type TMDs, such as  $\text{MoS}_2$ ,  $\text{WS}_2$ ,  $\text{MoSe}_2$  and  $\text{WSe}_2$  etc., the atomic displacements in  $\text{WTe}_2$  is relative complicated and disordered due to the lower symmetry. The related Raman tensor element ratios ( $b/a$ ), phase differences, and shrinkage degrees for the ten detected modes are summarized in Table 1. Here, we define the shrinkage degree as the ratio of the maximum intensity and its orthogonal direction intensity in a polar plot. Considering the absorption effect, we can obtain the

Experimental frequency (cm <sup>-1</sup> )	80	91	112	117	133	135	137	161	164	212
Irreducible representation	A <sub>1</sub>	A <sub>2</sub>	A <sub>2</sub>	A <sub>1</sub>	A <sub>1</sub>	A <sub>1</sub>	A <sub>1</sub>	A <sub>2</sub>	A <sub>1</sub>	A <sub>1</sub>
Calculated Frequency (cm <sup>-1</sup> )	75.5	90.8	113.7	115.4	131.1	133.2	135.5	164.4	163.7	209.1
Raman tensor elements ratio b/a	~0.71	–	–	~16.7	~0.30	~0.22	~0.10	–	~2.45	~0.49
cos ϕ <sub>ba</sub>	~1	–	–	~1	~1	~1	~1	–	~0.50	~0.68
Shrinkage degree	~1.98	~1.00	~1.00	~279	~11.1	~20.7	~100	~1.00	~3.72	~3.84

**Table 1.** The irreducible representations, calculated frequencies Raman tensor elements ratio  $b/a$ ,  $\cos \phi_{ba}$  and shrinkage degrees for all the detected phonon modes.

shrinkage degrees for  $A_1$  modes to be:  $\frac{|b|^2}{|a|^2} \left(1 + \frac{|b| \cos \phi_{ba} - 1}{2}\right)^{-1} |a| < |b|$  and  $\frac{|a|^2}{|b|^2} \left(1 + \frac{|b| \cos \phi_{ba} - 1}{2}\right) |a| > |b|$ , and those for  $A_2$  modes are closer to one. We find that the shrinkage degree reflects the vibrational tendency and complexity of detected modes. Specifically, the modes with smaller shrinkage degrees have the tendency to vibrate along the axes, and the ones with larger shrinkage degrees have the tendency to vibrate away from the axes. For three  $A_2$  modes, whose shrinkage degrees are close to one (minimum value), both W and Te atoms vibrate along the W-W chains ( $x$ -axis). In the case of  $A_1$  modes with relative small shrinkage degrees, for the  $A_1$  mode at  $\sim 80$  cm<sup>-1</sup>, all the W atoms have the tendency to vibrate along the  $z$  axis, and half of the Te atoms have the tendency to vibrate along the  $y$  axis. For the  $A_1$  mode at  $\sim 164$  cm<sup>-1</sup>, all the W (Te) atoms have the tendency to vibrate along the  $y$  ( $z$ ) axis. For the  $A_1$  mode at  $\sim 212$  cm<sup>-1</sup>, all the W (Te) atoms have the tendency to vibrate along the  $z$  ( $y$ ) axis. For the rest four  $A_1$  modes with larger shrinkage degrees, their vibrations are more complicated. This finding may be applied for studying the complicated atomic vibrations in other anisotropic materials.

## Conclusion

In this work, we study the ADPRS of WTe<sub>2</sub>. Ten Raman modes are clearly resolved. Their intensities show periodic variation with sample rotating. We identify the symmetries of these detected modes by quantitatively analyzing the ADPRS results using the symmetry selection rules based on the Raman tensors, and do the curve fitting to the angular dependent intensities of them using the complex Raman tensor elements induced by absorption effect. We also provide a rapid and nondestructive method to identify the crystallographic orientation of WTe<sub>2</sub>. We find that the defined shrinkage degree based on ADPRS also reflects the vibrational tendency and complexity of the detected modes, which is confirmed by their atomic vibrations calculated by density functional theory. Our work provides a deep understanding of the interaction between WTe<sub>2</sub> and light, which will benefit in future studies about the anisotropic optical, electrical, and mechanical properties of WTe<sub>2</sub> as well as other in-plane anisotropic materials.

## Methods

**Growth of bulk WTe<sub>2</sub>.** WTe<sub>2</sub> single crystals were grown by the CVT method<sup>8</sup>. Stoichiometric W and Te powders were ground together and loaded into a quartz tube with a small amount of TeBr<sub>4</sub> (transport agent). All weighing and mixing were carried out in a glove box. The tube was sealed under vacuum and placed in a two-zone furnace. The hot and cold zones were maintained at 800 °C and 700 °C, respectively, for 10 days. The crystal product appeared in cold zone.

**Measurements.** The quantitative atomic resolution force image of WTe<sub>2</sub> was measured by HR-AFM (Bruker Dimension Icon-PT). The angle- and polarization- resolved Raman spectra of exfoliated MoTe<sub>2</sub> on 300 nm SiO<sub>2</sub>/Si substrate were measured by a commercial micro-Raman system (Horiba Jobin Yvon HR800) under the backscattering geometry. In order to obtain high-resolution spectra, we used a 100× object lens, and the grating with 1800 or 2400 grooves/mm. The exposure time is 100 seconds. The excitation wavelength was 633 nm, and the light power was below 400 μW. The incident light was polarized along the horizontal direction. The parallel- and cross-polarized configurations were constructed by placing an analyzer before the spectrometer.

**Density Functional Calculations.** The calculations of phonon spectra were performed within local-density approximation (LDA) using projector-augmented wave potentials. A 3 × 2 × 1 supercell was created and the interatomic forces were computed using the Vienna ab initio simulation package code with the small displacements method<sup>40</sup>. From these, force constant matrices and phonon frequencies were extracted using the PHONOPY Code<sup>41</sup>. The kinetic energy cutoff of the plane-wave basis was set to be 350 eV and 3 × 2 × 2 Monkhorst Pack grid was used in the phonon calculation.

## References

- Zhang, Y., Tan, Y. W., Stormer, H. L. & Kim, P. Experimental observation of the quantum Hall effect and Berry's phase in graphene. *Nature* **438**, 201–204, doi: 10.1038/nature04235 (2005).
- Mak, K. F., He, K., Shan, J. & Heinz, T. F. Control of valley polarization in monolayer MoS<sub>2</sub> by optical helicity. *Nature nanotechnology* **7**, 494–498, doi: 10.1038/nnano.2012.96 (2012).
- Zhang, X. *et al.* Phonon and Raman scattering of two-dimensional transition metal dichalcogenides from monolayer, multilayer to bulk material. *Chemical Society Reviews* **44**, 2757–2785, doi: 10.1039/c4cs00282b (2015).
- Froehlicher, G. *et al.* Unified Description of the Optical Phonon Modes in N-Layer MoTe<sub>2</sub>. *Nano letters* **15**, 6481–6489, doi: 10.1021/acs.nanolett.5b02683 (2015).

5. Song, Q. J. *et al.* Physical origin of Davydov splitting and resonant Raman spectroscopy of Davydov components in multilayer MoTe<sub>2</sub>. *Physical Review B* **93**, doi: 10.1103/PhysRevB.93.115409 (2016).
6. Lee, C. H. *et al.* Tungsten Ditelluride: a layered semimetal. *Scientific reports* **5**, 10013, doi: 10.1038/srep10013 (2015).
7. Ali, M. N. *et al.* Large, non-saturating magnetoresistance in WTe<sub>2</sub>. *Nature* **514**, 205–208, doi: 10.1038/nature13763 (2014).
8. Pan, X. C. *et al.* Pressure-driven dome-shaped superconductivity and electronic structural evolution in tungsten ditelluride. *Nature communications* **6**, 7805, doi: 10.1038/ncomms 8805 (2015).
9. Pletikoscic, I., Ali, M. N., Fedorov, A. V., Cava, R. J. & Valla, T. Electronic structure basis for the extraordinary magnetoresistance in WTe<sub>2</sub>. *Physical Review Letters* **113**, 216601, doi: 10.1103/PhysRevLett.113.216601 (2014).
10. Soluyanov, A. A. *et al.* Type-II Weyl semimetals. *Nature* **527**, 495–498, doi: 10.1038/nature15768 (2015).
11. Kong, W. D. *et al.* Raman scattering investigation of large positive magnetoresistance material WTe<sub>2</sub>. *Applied Physics Letters* **106**, 081906, doi: 10.1063/1.4913680 (2015).
12. Jiang, Y. C., Gao, J. & Wang, L. Raman fingerprint for semi-metal WTe<sub>2</sub> evolving from bulk to monolayer. *Scientific reports* **6**, 19624, doi: 10.1038/srep19624 (2016).
13. Kim, Y. *et al.* Anomalous Raman scattering and lattice dynamics in mono- and few-layer WTe<sub>2</sub>. *Nanoscale* **8**, 2309–2316, doi: 10.1039/c5nr06098b (2016).
14. Lee, J. *et al.* Single- and few-layer WTe<sub>2</sub> and their suspended nanostructures: Raman signatures and nanomechanical resonances. *Nanoscale* **8**, 7854–7860, doi: 10.1039/c6nr00492j (2016).
15. Ribeiro, H. B. *et al.* Unusual Angular Dependence of the Raman Response in Black Phosphorus. *ACS Nano* **9**, 4270–4276, doi: 10.1021/acs.nano.5b00698 (2015).
16. Wu, J., Mao, N., Xie, L., Xu, H. & Zhang, J. Identifying the crystalline orientation of black phosphorus using angle-resolved polarized Raman spectroscopy. *Angewandte Chemie* **54**, 2366–2369, doi: 10.1002/anie.201410108 (2015).
17. Chenet, D. A. *et al.* In-Plane Anisotropy in Mono- and Few-Layer ReS<sub>2</sub> Probed by Raman Spectroscopy and Scanning Transmission Electron Microscopy. *Nano letters* **15**, 5667–5672, doi: 10.1021/acs.nanolett.5b00910 (2015).
18. Homes, C. C., Ali, M. N. & Cava, R. J. Optical properties of the perfectly compensated semimetal WTe<sub>2</sub>. *Physical Review B* **92**, 161109, doi: 10.1103/PhysRevB.92.161109 (2015).
19. Luo, Z. *et al.* Anisotropic in-plane thermal conductivity observed in few-layer black phosphorus. *Nature communications* **6**, 8572, doi: 10.1038/ncomms9572 (2015).
20. Tao, J. *et al.* Mechanical and Electrical Anisotropy of Few-Layer Black Phosphorus. *ACS Nano* **9**, 11362–11370, doi: 10.1021/acs.nano.5b05151 (2015).
21. Fei, R. & Yang, L. Strain-engineering the anisotropic electrical conductance of few-layer black phosphorus. *Nano letters* **14**, 2884–2889, doi: 10.1021/nl500935z (2014).
22. Liu, E. *et al.* Integrated digital inverters based on two-dimensional anisotropic ReS<sub>2</sub> field-effect transistors. *Nature communications* **6**, 6991, doi: 10.1038/ncomms7991 (2015).
23. Xia, F., Wang, H. & Jia, Y. Rediscovering black phosphorus as an anisotropic layered material for optoelectronics and electronics. *Nature communications* **5**, 4458, doi: 10.1038/ncomms5458 (2014).
24. Lin, Y. C. *et al.* Single-Layer ReS<sub>2</sub>: Two-Dimensional Semiconductor with Tunable In-Plane Anisotropy. *ACS Nano* **9**, 11249–11257, doi: 10.1021/acs.nano.5b04851 (2015).
25. Aslan, O. B. *et al.* Linearly Polarized Excitons in Single- and Few-Layer ReS<sub>2</sub> Crystals. *ACS Photonics* **3**, 96–101, doi: 10.1021/acsp Photonics.5b00486 (2015).
26. Wolverson, D. *et al.* Raman Spectra of Monolayer, Few-Layer, and Bulk ReSe<sub>2</sub>: An Anisotropic Layered Semiconductor. *ACS Nano* **8**, 11154–11164, doi: 10.1021/nn5053926 (2014).
27. Zhao, H. *et al.* Interlayer interactions in anisotropic atomically thin rhenium diselenide. *Nano Research* **8**, 3651–3661, doi: 10.1007/s12274-015-0865-0 (2015).
28. Zhang, E. *et al.* ReS<sub>2</sub>-Based Field-Effect Transistors and Photodetectors. *Advanced Functional Materials* **25**, 4076–4082, doi: 10.1002/adfm.201500969 (2015).
29. Zhong, H.-X., Gao, S., Shi, J.-J. & Yang, L. Quasiparticle band gaps, excitonic effects, and anisotropic optical properties of the monolayer distorted 1T diamond-chain structures ReS<sub>2</sub> and ReSe<sub>2</sub>. *Physical Review B* **92**, doi: 10.1103/PhysRevB.92.115438 (2015).
30. Nagler, P., Plechinger, G., Schüller, C. & Korn, T. Observation of anisotropic interlayer Raman modes in few-layer ReS<sub>2</sub>. *physica status solidi (RRL) - Rapid Research Letters* **10**, 185–189, doi: 10.1002/pssr.201510412 (2015).
31. He, R. *et al.* Coupling and Stacking Order of ReS<sub>2</sub> Atomic Layers Revealed by Ultralow-Frequency Raman Spectroscopy. *Nano letters*, **16**, 1404–1409, doi: 10.1021/acs.nanolett.5b04925 (2016).
32. Liu, E. *et al.* High responsivity phototransistors based on few-layer ReS<sub>2</sub> for weak signal detection. *Nature communication* **6**, 6991, doi: 10.1038/ncomms7991 (2015).
33. Qiao, X. F. *et al.* Polytypism and Unexpected Strong Interlayer Coupling of two-Dimensional Layered ReS<sub>2</sub>. *Nanoscale*, **8**, 8324–8332, doi: 10.1039/C6NR01569G (2016).
34. Ling, X. *et al.* Anisotropic Electron-Photon and Electron-Phonon Interactions in Black Phosphorus. *Nano letters* **16**, 2260–2267, doi: 10.1021/acs.nanolett.5b04540 (2016).
35. Lorchat, E., Froehlicher, G. & Berciaud, S. Splitting of Interlayer Shear Modes and Photon Energy Dependent Anisotropic Raman Response in N-Layer ReSe<sub>2</sub> and ReS<sub>2</sub>. *ACS Nano* **10**, 2752–2760, doi: 10.1021/acs.nano.5b07844 (2016).
36. Boneschanscher, M. P. *et al.* Quantitative Atomic Resolution Force Imaging on Epitaxial Graphene with Reactive and Nonreactive AFM Probes. *ACS Nano* **6**, 10216–10221, doi: 10.1021/nn3040155 (2012).
37. Mar, A., Jobic, S. & Ibers, J. A. Metal-Metal vs Tellurium-Tellurium Bonding in WTe<sub>2</sub> and Its Ternary Variants TaIrTe<sub>4</sub> and NbIrTe<sub>4</sub>. *J. Am. Chem. Soc.* **114**, 8963–8971 (1992).
38. Loudon, R. The Raman effect in crystals. *Advances in Physics* **13**, 423–482, doi: 10.1080/00018736400101051 (1964).
39. Cardona, M. In *Light Scattering in Solids II*. Vol. 50, Ch. 2, 19–278 (Springer, 1982).
40. Kresse, G., Furthmüller, J. & Hafner, J. Ab initio Force Constant Approach to Phonon Dispersion Relations of Diamond and Graphite. *Europhys. Lett.* **32**, 729–734 (1995).
41. Togo, A., Oba, F. & Tanaka, I. First-principles calculations of the ferroelastic transition between rutile-type and CaCl<sub>2</sub>-type SiO<sub>2</sub> at high pressures. *Physical Review B* **78**, 134106, doi: 10.1103/PhysRevB.78.134106 (2008).

## Acknowledgements

We acknowledge support from the National Key Projects for Basic Research Program of China (2013CB921901, 2012CB932703, 2013CB922103, and 2011CB922103), the National Natural Science Foundation of China (Grants nos 61521004, 61125402, 51172004, 11474007, 11225421, 11434010, 11474277, 91421109, 11134005, 61176088, 11522432, 11525417, 11274003, 61176079, 21373156 and 11404253).

## Author Contributions

Q.S. and L.D. designed the experiments and did the analysis. X.P. and F.S. grew the bulk WTe<sub>2</sub> sample. H.W., P.L. and X.W. did the density functional calculations. Q.S., K.Z., Q.T., X.X., M.L. and L.D. contributed to the Raman



measurements. Q.S., Yi Wan and Yilun Wang contributed to the measurements of atomic force microscope. Q.S. and L.D. wrote the paper and all authors helped with the revisions. We also thank Prof. Pingheng Tan from the Institute of Semiconductors, Chinese Academy of Sciences for helpful discussion.

### Additional Information

**Supplementary information** accompanies this paper at <http://www.nature.com/srep>

**Competing financial interests:** The authors declare no competing financial interests.

**How to cite this article:** Song, Q. *et al.* The In-Plane Anisotropy of  $WTe_2$  Investigated by Angle-Dependent and Polarized Raman Spectroscopy. *Sci. Rep.* **6**, 29254; doi: 10.1038/srep29254 (2016).



This work is licensed under a Creative Commons Attribution 4.0 International License. The images or other third party material in this article are included in the article's Creative Commons license, unless indicated otherwise in the credit line; if the material is not included under the Creative Commons license, users will need to obtain permission from the license holder to reproduce the material. To view a copy of this license, visit <http://creativecommons.org/licenses/by/4.0/>